

# Mesoporous N-Doped Carbons Prepared with Thermally Removable Nanoparticle Templates: An Efficient Electrocatalyst for Oxygen Reduction Reaction

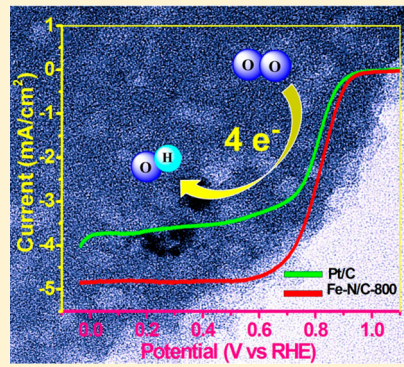
Wenhan Niu,<sup>†</sup> Ligui Li,<sup>\*,†</sup> Xiaojun Liu,<sup>†</sup> Nan Wang,<sup>†</sup> Ji Liu,<sup>†</sup> Weijia Zhou,<sup>†</sup> Zhenghua Tang,<sup>†</sup> and Shaowei Chen<sup>\*,†,‡</sup>

<sup>†</sup>New Energy Research Institute, School of Environment and Energy, South China University of Technology, Guangzhou Higher Education Mega Centre, Guangzhou 510006, China

<sup>‡</sup>Department of Chemistry and Biochemistry, University of California, 1156 High Street, Santa Cruz, California 95064, United States

## S Supporting Information

**ABSTRACT:** Thermally removable nanoparticle templates were used for the fabrication of self-supported N-doped mesoporous carbons with a trace amount of Fe (Fe-N/C). Experimentally Fe-N/C was prepared by pyrolysis of poly(2-fluoroaniline) (P2FANI) containing a number of FeO(OH) nanorods that were prepared by a one-pot hydrothermal synthesis and homogeneously distributed within the polymer matrix. The FeO(OH) nanocrystals acted as rigid templates to prevent the collapse of P2FANI during the carbonization process, where a mesoporous skeleton was formed with a medium surface area of about  $400 \text{ m}^2/\text{g}$ . Subsequent thermal treatments at elevated temperatures led to the decomposition and evaporation of the FeO(OH) nanocrystals and the formation of mesoporous carbons with the surface area markedly enhanced to  $934.8 \text{ m}^2/\text{g}$ . Electrochemical measurements revealed that the resulting mesoporous carbons exhibited apparent electrocatalytic activity for oxygen reduction reactions (ORR), and the one prepared at  $800^\circ\text{C}$  (Fe-N/C-800) was the best among the series, with a more positive onset potential ( $+0.98 \text{ V}$  vs RHE), higher diffusion-limited current, higher selectivity (number of electron transfer  $n > 3.95$  at  $+0.75 \text{ V}$  vs RHE), much higher stability, and stronger tolerance against methanol crossover than commercial Pt/C catalysts in a  $0.1 \text{ M KOH}$  solution. The remarkable ORR performance was attributed to the high surface area and sufficient exposure of electrocatalytically active sites that arose primarily from N-doped carbons with minor contributions from Fe-containing species.



## INTRODUCTION

In proton exchange membrane fuel cells (PEMFCs), small molecule fuels are oxidized at the anode, and concurrently oxygen is reduced at the cathode. Of these, the sluggish kinetics of oxygen reduction reaction (ORR) at the cathode greatly limits the energy conversion efficiency of fuel cells. For practical applications, a sufficiently high current density is generally needed. Thus, noble metals (e.g., Pt, Pd, Ru, etc.) and their alloy nanoparticles have been used extensively as effective catalysts for both anodic and cathodic reactions.<sup>1–4</sup> However, the high costs, poor durability, and low poison resistance of these noble metals-based catalysts have been the main bottlenecks that hamper the widespread commercialization of PEMFCs.<sup>5–8</sup> Extensive research efforts have therefore been devoted to the development of cost-effective alternatives, in particular, nonprecious-metal catalysts (NPMCs) for ORR.<sup>6,9–12</sup>

Thus far, (nano)composites based on transition metals and nitrogen-doped carbons (M-N/C, with M = Fe, Co, etc.)<sup>13–19</sup> have been considered as the most promising NPMCs for ORR. Although the nature of the active sites in M-N/C catalysts is still not fully understood and it may vary between different M-

N/C catalysts, it has been found that the specific surface area and structure of the catalysts largely determine the accessibility of the active sites and hence the eventual electrocatalytic performance.<sup>13,20,21</sup> Within this context, it is of paramount significance to maximize the electrochemical surface area, especially the contribution from mesopores (2–50 nm), such that the transport of ORR-relevant species (e.g.,  $\text{H}^+$ ,  $\text{OH}^-$ ,  $\text{O}_2$ ,  $\text{H}_2\text{O}$ , etc.) may be facilitated and the ORR catalytic activity be enhanced and even optimized.<sup>9</sup> Toward this goal, several methods have been reported in the literature in the preparation of highly porous carbons.<sup>13,22–25</sup> Of these, direct carbonization of porous precursors such as metal–organic frameworks (MOFs) is considered as a promising method to prepare M-N/C with controlled pore structures.<sup>23,26</sup> However, the resulting surface area is generally rather low probably because of collapse of pores at elevated temperatures.<sup>27</sup>

To mitigate the collapse/agglomeration problem, rigid templates are typically used during carbonization, such as silica nanoparticles<sup>21</sup> and anodic porous alumina;<sup>28</sup> and porous

Received: February 24, 2015

Published: April 10, 2015



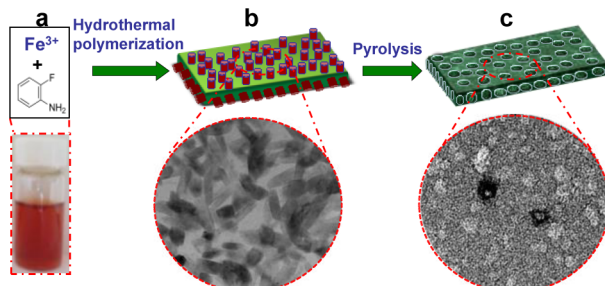
carbon-based catalysts have indeed been prepared with a remarkably high surface area and ORR activity. However, in these prior studies, the “rigid template” approaches inevitably involve several complicated and tedious processes, such as synthesis and dispersion of monodisperse template nanoparticles in precursor matrices, postsynthesis removal of excess template particles, and sample purification. These complicate the preparation of high-performance catalysts and eventually hinder the scale-up production and cost reduction of the catalysts. In addition, the catalytic activity may suffer because part of the active sites may be inevitably lost in the postsynthesis removal of excess templates through acidic/basic etching. Therefore, an immediate question arises. Is it possible to embed homogeneous “rigid templates” within the precursor matrices where calcination at elevated temperatures leads to the ready formation of mesoporous carbons with a high surface area and concurrently effective removal of the template particles? This is the primary motivation of the present work.

Herein, we report a novel route to the fabrication of mesoporous Fe-N/C catalysts by controlled pyrolysis of a poly(2-fluoroaniline) (P2FANI) matrix within which FeO(OH) nanorods were homogeneously embedded. The FeO(OH) nanocrystals acted not only as rigid templates to prevent the collapse of P2FANI during carbonization but also facilitated the formation of mesopores/cavities in the carbonized skeletons by thermal decomposition and evaporation at high temperatures (600–900 °C). The resulting mesoporous Fe-N/C exhibited a specific surface area up to 934.8 m<sup>2</sup>/g. Electrochemical measurements showed that the nanocomposites exhibited remarkable ORR activity in alkaline media. The best catalyst among the series was identified as the sample prepared at 800 °C, which featured an onset potential that was 22 mV more positive, a higher diffusion-limited current, larger electron-transfer number ( $n > 3.95$ ) even at low overpotentials, substantially longer durability, and stronger poison resistance than state-of-the art commercial Pt/C catalysts. These results demonstrate that the mesoporous Fe-N/C prepared by sacrificial FeO(OH) nanocrystals might be a viable ORR catalyst for high-performance PEMFCs.

## EXPERIMENTAL SECTION

**Synthesis of Fe-N/C Hybrids.** As depicted in Scheme 1, in a typical synthesis, 6 mmol of 2-fluoroaniline (2FANI) and 12 mmol of FeCl<sub>3</sub> (i.e., the molar feed ratio of FeCl<sub>3</sub>:2FANI was 2:1) were mixed in 20 mL of deionized water for about 10 min. The color of the

**Scheme 1. Schematic of the Preparation Process of Fe-N/C Catalysts<sup>a</sup>**



<sup>a</sup>(a) Aqueous solution of 2-fluoroaniline and FeCl<sub>3</sub>; (b) hybrid products of FeO(OH) nanocrystals and poly(2-fluoroaniline) prepared by hydrothermal polymerization; and (c) Fe-N/C powders obtained by pyrolysis in a N<sub>2</sub> atmosphere at controlled temperatures.

solution gradually changed from yellow to dark brown due to the formation of Fe(OH)<sub>3</sub> from hydrolysis of FeCl<sub>3</sub>. Subsequently, the solution was transferred to a sealed Teflon-lined autoclave and heated at 180 °C for 4 h. The resulting precipitate (denoted as Fe-N/C-precursor) at the bottom of the autoclave was collected and dried after extensive washing with ethanol and deionized water. Finally, the dried Fe-N/C-precursor was pyrolyzed at controlled temperatures (600, 700, 800, or 900 °C) for 2 h in a N<sub>2</sub> atmosphere at the gas flow rate of 300 sccm. The final products were referred to as Fe-N/C-T with  $T$  being the calcination temperature.

For comparison, a series of Fe-N/C-800 composites were also prepared via the same procedure except that the molar feed ratio of FeCl<sub>3</sub> to 2FANI was changed to 0.5:1, 1:1, and 5:1, respectively.

**Characterizations.** Transmission electron microscopic (TEM) measurements were conducted on a Tecnai G2-F20 equipped with an EDS detector at an acceleration voltage of 100 kV. TEM samples were prepared by dropcasting a catalyst dispersion directly onto a copper grid coated with a holey carbon film. Scanning electron microscopic (SEM) images were acquired on a field-emission scanning electron microscope (S-4800, Hitachi). X-ray photoelectron spectroscopic (XPS) measurements were performed on a Thermo Escalab 250Xi instrument. Powder X-ray diffraction (XRD) patterns were recorded with a Bruker D8-Advance diffractometer using Cu K $\alpha$  radiation. Thermogravimetric analysis (TGA) was performed on a METTLER instruments under a N<sub>2</sub> atmosphere at a heating rate of 5 °C/min. Brunauer–Emmet–Teller (BET) surface area was determined by using a Micromeritics ASAP 2010 instrument with nitrogen adsorption at 77 K using the Barrett–Joyner–Halenda (BJH) method. Raman spectra were recorded on a RENISHAW inVia instrument with an Ar laser source of 488 nm in a macroscopic configuration.

**Electrochemistry.** Electrochemical measurements were performed on a CHI 750E electrochemical workstation (CH Instruments, Chenzhuo Co., China) in a conventional three-electrode cell, with a platinum wire as the counter electrode, a Ag/AgCl as the reference electrode, and a catalysts-modified glassy carbon electrode (GCE) as the working electrode. The catalyst ink was prepared by adding 1 mg of a catalyst into a solution containing water, isopropanol, and Nafion (5%) at a volume ratio of 4:1:0.025 to form a homogeneous suspension at the catalyst concentration of 0.78 mg/mL. A calculated amount (20  $\mu$ L) of the suspension was then evenly cast on the clean GCE surface with a syringe and dried in air, corresponding to a catalyst loading of 79.6  $\mu$ g/cm<sup>2</sup>. Linear sweep voltammograms (LSV) were acquired in an O<sub>2</sub>-saturated 0.1 M KOH aqueous solution at various rotation rates (400–2025 rpm).

In the measurements, the Ag/AgCl reference electrode was calibrated with respect to a reversible hydrogen electrode (RHE). The calibration was performed in a high-purity H<sub>2</sub> (99.999%) saturated electrolyte with two Pt wires as the working and counter electrode, respectively. Cyclic voltammograms (CV) were acquired at a potential scan rate of 1 mV/s, and the average of the two potentials at which the current crossed zero was taken as the thermodynamic potential of the RHE.<sup>22,25</sup> In 0.1 M KOH,  $E_{\text{Ag}/\text{AgCl}} = E_{\text{RHE}} + 0.964$  V.

## RESULTS AND DISCUSSION

The structures of the Fe-N/C samples prepared above were first examined by TEM and SEM measurements. One can see that the Fe-N/C-precursor, prepared by a low-temperature hydrothermal process of 2FANI and FeCl<sub>3</sub> (Scheme 1), exhibited a largely sheet-like morphology (Figure S1), within which a number of rod-like nanocrystals (12–75 nm in width and 30–125 nm in length) were rather evenly distributed on a low contrast background that was most likely P2FANI, as depicted in Figure 1a (and Figure S2). HRTEM measurements (Figure 1b) showed well-defined lattice fringes of the nanorod crystals, where the lattice spacings of 0.125 and 0.138 nm were consistent with the (331) and (330) crystalline planes of goethite phase FeO(OH), respectively. Consistent results were obtained in XRD measurements which showed a series of well-

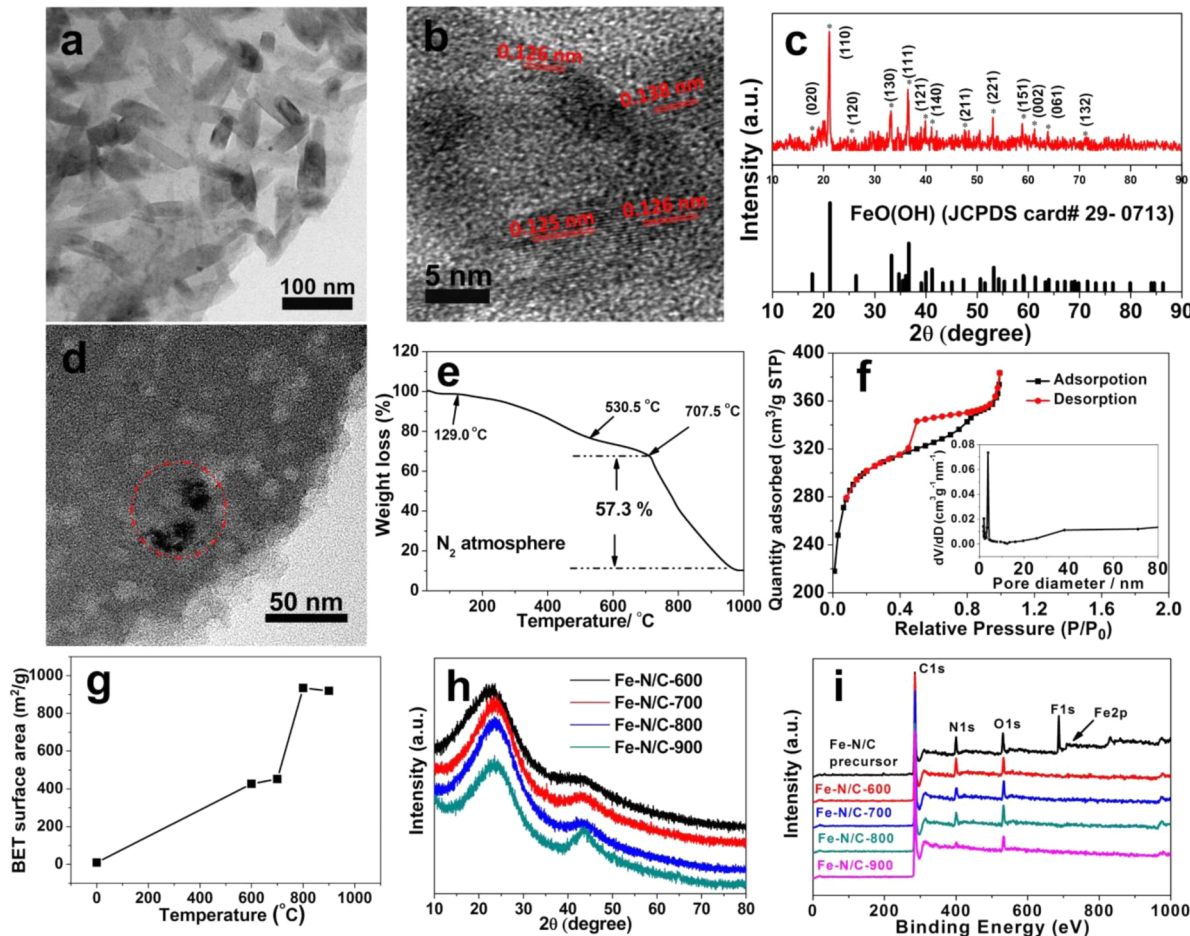


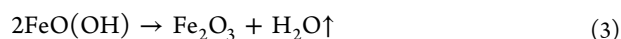
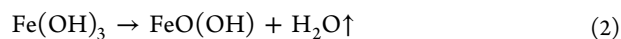
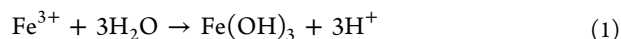
**Figure 1.** (a) Representative TEM image, (b) high-resolution TEM image, and (c) XRD patterns of Fe-N/C-precursor where FeO(OH) nanocrystals were embedded within the P2FANI matrix. (d) Representative TEM image of Fe-N/C-800, (e) TGA curve of Fe-N/C-precursor, and (f) N<sub>2</sub> adsorption/desorption isotherm of Fe-N/C-800. (g) BET surface areas (inset to panel (f) is the corresponding pore size distribution), (h) XRD patterns, and (i) XPS survey spectra of the series of Fe-N/C-T samples ( $T = 600, 700, 800$ , and  $900$ ).

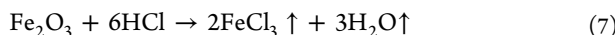
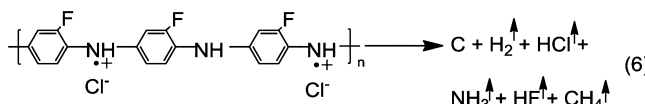
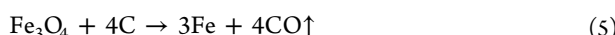
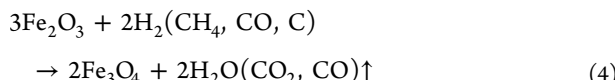
defined diffraction peaks at  $2\theta = 17.8^\circ, 21.2^\circ, 33.2^\circ, 36.6^\circ$ , and  $39.9^\circ$ . These are consistent with the (020), (110), (130), (111), and (121) crystalline planes of FeO(OH) (JCPDS card no. 29-0713), respectively (Figure 1c). Taken together, these results indicate the ready formation of a P2FANI-FeO(OH) composite with FeO(OH) nanorods embedded within the polymer matrix by a simple one-pot hydrothermal synthesis (Scheme 1).

After thermal treatment of the Fe-N/C-precursor at elevated temperatures, striking changes of the morphology were observed. For instance, for Fe-N/C-800 that was depicted in Figure 1d, the rod-like FeO(OH) nanocrystals disappeared completely, and only a small number of dark-contrast domains (highlighted by the red dashed circle) remained in the gray carbon matrix. Selected-area EDS analysis showed that the Fe element could be observed only in the dark-contrast spots and was absent elsewhere (Figure S3), indicating that the majority of the FeO(OH) nanorods were removed effectively during the high-temperature carbonization process and the dark spots mostly likely comprised of residuals from the FeO(OH) nanorods. Second, one can see that a large number of low-contrast cavities were formed and distributed rather evenly throughout the samples, with the diameter in the range from 10 to 60 nm (signifying the formation of mesopores), highly comparable to the width of the FeO(OH) nanorods. Therefore, it is very likely that these cavities actually resulted from the

thermal decomposition and removal of the FeO(OH) nanocrystals.<sup>29–31</sup>

To better understand the formation process of mesopores in Fe-N/C, TGA measurements were carried out with Fe-N/C-precursor in a N<sub>2</sub> atmosphere. As depicted in Figure 1e, three major steps of weight loss can be observed. The first weight loss was very small, starting at below 129.0 °C, which most likely resulted from the loss of adsorbed H<sub>2</sub>O, while the second weight loss was rather significant at 21.8% between 129.0 and 530.5 °C, which was likely due to the decomposition of low molecular weight polymers or oligomers of 2-fluoroaniline, followed by H<sub>2</sub>O released from FeO(OH) at 530.5–707.5 °C. The third weight loss of 57.3% started at 707.5 °C and ended at around 1000 °C, which was most probably due to the decomposition of high molecular weight polymers and concurrently the evaporation of FeCl<sub>3</sub>.<sup>32</sup> The mechanism likely involves the following reactions:<sup>32</sup>





At the beginning,  $\text{FeCl}_3$  was hydrolyzed into amorphous  $\text{Fe(OH)}_3$  in the presence of alkaline 2-fluoroaniline (eq 1), and 2-fluoroaniline was protonated by hydrochloric acid resulting from  $\text{FeCl}_3$  hydrolysis. Hydrothermal polymerization of the protonated 2-fluoroaniline resulted in the formation of sheet-like P2FANI aggregates doped by hydrochloric acid. With amorphous  $\text{Fe(OH)}_3$  mixed homogeneously with protonated 2-fluoroaniline, hydrothermal polymerization led to the generation of  $\text{FeO(OH)}$  nanocrystals from  $\text{Fe(OH)}_3$  (eq 2) that were evenly distributed within the polymer matrix. In low-temperature pyrolysis (below 700 °C), the  $\text{FeO(OH)}$  nanocrystals were converted to  $\text{Fe}_2\text{O}_3$  (eq 3), along with degradation of low molecular weight polymers. At higher temperatures (>700 °C), high molecular weight polymers were degraded to graphitic carbons, which was accompanied by the generation of a series of volatile species such as hydrofluoric acid, hydrochloric acid, ammonia, hydrogen, and methane (eqs 4–6).<sup>33–35</sup> HCl then reacted with  $\text{Fe}_2\text{O}_3$  to form volatile  $\text{FeCl}_3$  (eq 7), leading to the appearance of a sudden weight loss (the weight fraction of  $\text{FeO(OH)}$  in Fe-N/C-precursor was evaluated to be ca. 75%, Table S1) and consequently the formation of a number of cavities/holes in the carbon matrix, as observed in TEM (Figure 1d) and EDS (Figure S3) measurements. That is, in the present study,  $\text{FeO(OH)}$  nanorods actually served as thermally removable templates which not only helped prevent the collapse of the polymer matrix during carbonization but also facilitated the formation of mesopores in the carbon skeletons.

The formation of carbon skeletons was confirmed by Raman measurements where the graphitic D and G bands can be clearly seen at ca. 1365 and 1576 cm<sup>-1</sup>, respectively, for all examples (Figure S4).<sup>36,37</sup> In addition, the ratio of the D and G band intensities ( $I_{\text{D}}/I_{\text{G}}$ ) of the nanocomposites varied slightly with the pyrolysis temperature at 0.84 for Fe-N/C-600, 0.94 for Fe-N/C-700, 0.91 for Fe-N/C-800, and 0.90 for Fe-N/C-900. That is, with an increase of the pyrolysis temperature from 600 to 700 °C, the formation of graphitic carbon was enhanced;<sup>38</sup> at higher carbonization temperatures (up to 900 °C), the  $I_{\text{D}}/I_{\text{G}}$  ratio was almost invariant, suggesting a consistent carbon molecular skeleton among the samples.<sup>39</sup>

BET analyses were then performed to investigate the specific surface area and pore size of the carbon materials. Figure 1f shows the  $\text{N}_2$  adsorption/desorption isotherm of Fe-N/C-800, from which the corresponding specific surface area was estimated to be 934.8 m<sup>2</sup>/g and the pore size distributions (figure inset) suggested the formation of mesopores with the pore diameter in the range from 3.8 to 38.6 nm (results for other samples are shown in Figure S5). Notably, the surface area is highly dependent on the pyrolysis temperature. As shown in Figure 1g, the apparent surface area was only 9.4 m<sup>2</sup>/g for the Fe-N/C-precursor; yet after pyrolysis at 600–700 °C,

it increased markedly to about 430 m<sup>2</sup>/g (Fe-N/C-600 and Fe-N/C-700). For the Fe-N/C-800, the BET surface area exhibited a further increase to 934.8 m<sup>2</sup>/g, whereas at even higher pyrolysis temperatures (900 °C), the BET surface area actually decreased slightly, likely due to partial collapse of the graphitic skeleton. That is, the specific surface area reached the maximum when the sample was prepared at 800 °C.

The crystalline structures of the Fe-N/C-T composites were then studied by XRD measurements. Figure 1h depicts the XRD patterns of the four Fe-N/C-T ( $T = 600, 700, 800$ , and 900) samples. It can be seen that Fe-N/C-600 (black curve) exhibited two main diffraction peaks at  $2\theta = 23.0^\circ$  and  $44.0^\circ$ , which may be ascribed to diffractions from the (002) and (101) crystalline planes of graphite carbon, respectively. At increasing pyrolysis temperatures, these two peaks appear at a somewhat higher  $2\theta$  angles and become stronger and narrower, indicating the formation of an increasingly ordered graphitic structure. Note that no diffraction patterns of crystalline  $\text{Fe}_3\text{O}_4$ ,  $\text{Fe}_2\text{O}_3$ , or Fe can be observed, signifying that most of the Fe-containing species have been effectively removed during high-temperature pyrolysis (Figure S3). In fact, from XPS measurements (Figure 1i), one can see that whereas the F 1s and Fe 2p peaks were clearly defined in the Fe-N/C-precursor sample (black curve), pyrolysis treatments at elevated temperatures (600–900 °C) led to almost complete disappearance of these two elements, with only N, C, and O remaining in the samples (Table S1).

Nitrogen-bonding configurations and Fe contents in the porous carbons were then quantitatively analyzed by high-resolution XPS measurements. As shown in Figures 2a and S6,

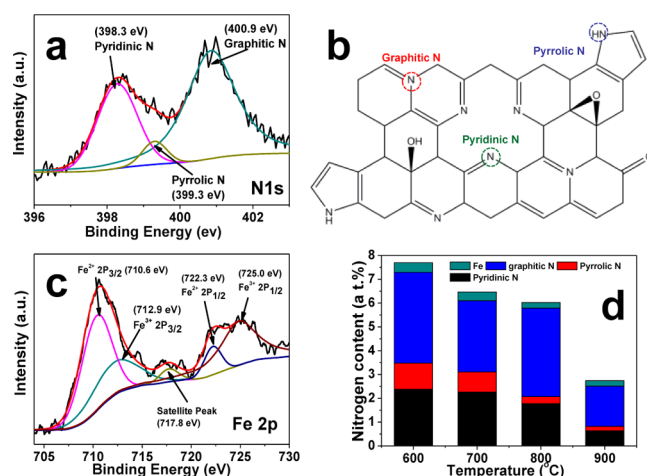


**Figure 2.** High-resolution scans of (a) N 1s and (c) Fe 2p electrons in Fe-N/C-800. (b) Illustration of three types of nitrogen in graphene. (d) Concentrations of Fe and N dopants in Fe-N/C prepared at different temperatures.

the N 1s spectra can be deconvoluted into three peaks at 398.0, 399.3, and 400.9 eV, which are consistent with pyridinic N, pyrrolic N and graphitic N (Figure 2b), respectively, suggesting that nitrogen was indeed doped into the carbon molecular skeletons.<sup>36,40,41</sup> Note that pyridinic and pyrrolic nitrogens might coordinate with Fe to form  $\text{Fe-N}_x$  moieties,<sup>14,42</sup> and pyridinic N and graphitic N are generally considered as the efficient active sites for ORR.<sup>8,14,18</sup> In addition, based on the integrated peak areas, the concentrations of the different nitrogen dopants were quantified (Table S1), where it can be seen that graphitic-N was the dominated species in all samples,

and the concentration was the highest at 3.72 at. % with Fe-N/C-800 among the series (Figure 2d), whereas the loadings of pyridinic and pyrrolic nitrogens were much lower and diminished markedly with increasing pyrolysis temperature (Table S1). This signifies decreasing thermal stability of pyridinic-N and pyrrolic-N as compared with graphitic-N.<sup>43</sup> Furthermore, Figure 2c shows the high-resolution scan of Fe 2p electrons, where deconvolution yielded two pairs of peaks for Fe<sup>2+</sup> (710.6 and 722.3 eV) and Fe<sup>3+</sup> (712.9 and 725.0 eV), with a satellite peak at 717.8 eV.<sup>14</sup> Based on the integrated peak areas, the Fe atomic fraction was quantitatively estimated and found to decrease from 0.52 at. % for the Fe-N/C-precursor sample to 0.41 at. % for Fe-N/C-600, 0.36 at. % for Fe-N/C-700, and 0.24 at. % for Fe-N/C-800 and Fe-N/C-900 (Figure 2d and Table S1), consistent with the formation of volatile iron compounds, most probably FeCl<sub>3</sub> (eq 7), during pyrolysis.

Interestingly, the resulting Fe-N/C samples exhibited remarkable electrocatalytic activity for ORR. Figure 3 depicts

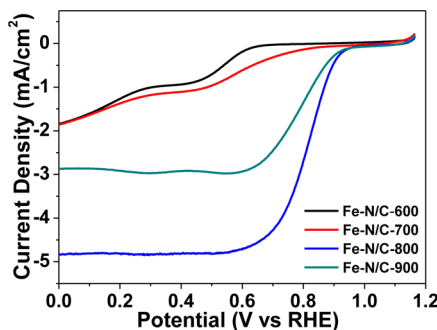


**Figure 3.** Rotating disk electrode (RDE) voltammograms of a GCE modified with 79.6  $\mu\text{g}/\text{cm}^2$  of Fe-N/C-T ( $T = 600, 700, 800$ , and  $900$ ) in an  $\text{O}_2$ -saturated 0.1 M KOH solution at a rotation speed of 1600 rpm. Potential sweep rate 10 mV/s.

the RDE voltammograms for the four samples prepared at different pyrolysis temperatures. One can see that for the Fe-N/C-600 sample, nonzero cathodic current started to appear when the electrode potential was swept negatively and reached +0.68 V (vs RHE); however, for Fe-N/C-700, the onset potential was much more positive at +0.87 V, and for Fe-N/C-800 and Fe-N/C-900, it was even more positive at +0.98 V and +0.96 V, respectively. Concurrently, the limiting currents also exhibited an apparent variation among the samples. For instance, at +0.45 V, the limiting currents were 0.86 mA/cm<sup>2</sup> for Fe-N/C-600, 1.06 mA/cm<sup>2</sup> for Fe-N/C-700, 4.81 mA/cm<sup>2</sup> for Fe-N/C-800, and 2.92 mA/cm<sup>2</sup> for Fe-N/C-900, signifying that the Fe-N/C-800 sample stood out as the best ORR catalyst among the series. Consistent behaviors were observed in cyclic voltammetric (Figure S7) and RRDE (Figure S8) measurements. Interestingly, this coincided with the highest concentration of graphitic-N and surface area in the Fe-N/C-800 sample (Figure 2d and Table S1), suggesting that graphitic nitrogen likely played a dominant role in the determination of the ORR activity.

The ORR activities of Fe-N/C-800 were actually even better than that of commercial Pt/C (20 wt %) at the same mass loading. As depicted in Figure 4a, whereas only featureless double-layer charging current was observed in N<sub>2</sub>-saturated 0.1 M KOH within the potential range from -0.04 V to +1.16 V, the Fe-N/C-800-modified electrode (top) exhibited an apparent cathodic peak at +0.81 V (vs RHE) when the

solution was saturated with O<sub>2</sub>. For Pt/C catalysts (bottom curves), the oxygen reduction peak appeared at almost the same potential position. Yet, the peak current density was markedly higher for Fe-N/C-800 (1.51 mA/cm<sup>2</sup>) than that for Pt/C (1.20 mA/cm<sup>2</sup>). In fact, the ORR performance of Fe-N/C-800 was even better than, or at least comparable to leading results of M-N/C catalysts reported in recent studies (Table S2).

Consistent results were obtained in RRDE voltammetric measurements. Figure 4b depicts the linear polarization curves of a GCE modified with Fe-N/C-800 (red curves) and Pt/C (black curves), where the onset potential was identified at +0.98 V for the former and +0.95 V for the latter. Note that these are substantially more positive than that (+0.923 V) observed in a recent study where Fe and N codoped carbons were prepared by pyrolysis of an iron-coordinated polymer complex (Table S2).<sup>14,44</sup> The diffusion-limited current also suggested a better performance of Fe-N/C-800 (e.g., 4.81 mA/cm<sup>2</sup> at +0.40 V at 1600 rpm) than that of Pt/C (3.50 mA/cm<sup>2</sup>). The superior electrocatalytic activity of Fe-N/C-800 was further confirmed by the number of electron transfer ( $n$ , eq 8a) and the H<sub>2</sub>O<sub>2</sub> percent yield (eq 8b) involved in ORR,

$$n = \frac{4I_{\text{disk}}}{I_{\text{ring}}/N + I_{\text{disk}}} \quad (8a)$$

$$\text{H}_2\text{O}_2\% = \frac{200I_{\text{ring}}/N}{I_{\text{ring}}/N + I_{\text{disk}}} \quad (8b)$$

where  $N$  is the collection efficiency (37%) and  $I_{\text{disk}}$  and  $I_{\text{ring}}$  are the voltammetric currents at the disk and ring electrodes, respectively. As shown in Figure 4c, for the Fe-N/C-800, the H<sub>2</sub>O<sub>2</sub> yield was <5% in the low overpotential range from +0.50 to +0.80 V, and the average  $n$  was ca. 3.95, slightly higher than that of Pt/C ( $n = 3.90$ ).

From the RRDE voltammograms in Figure 4d, it can be seen that the limiting currents of the Fe-N/C-800 electrode increased with increasing rotation speed (from 400 to 2025 rpm). The corresponding Koutecky-Levich (K-L) plots within the potential range from +0.49 to +0.69 V exhibit good linearity with a rather consistent slope, suggesting first-order reaction kinetics for ORR with respect to oxygen concentration in the solution (inset to Figure 4d). The corresponding Tafel plots are shown in Figure 4e, where a similar slope was observed for Fe-N/C-800 (59 mV/dec) and Pt/C (62 mV/dec), suggesting a similar reaction mechanism of ORR on the catalyst surface where the rate-determining step at both catalysts was likely the first electron reduction of oxygen. Importantly, within this potential range from +0.65 to +0.95 V, the specific activity of Fe-N/C-800 was apparently higher than that of Pt/C.

Since the porous carbons obtained above were codoped with Fe and N, one may wonder what roles these two dopants played in determining the electrocatalytic activity. Previously two mechanisms have been proposed to account for the ORR activity of M-N/C catalysts.<sup>45,46</sup> One involves the M-N<sub>x</sub> moieties, and the other is the N dopants within the carbon matrix.<sup>47</sup> Therefore, in the present study, a series of further experiments were conducted to identify the active sites in the resulting porous carbons for ORR. It is well-known that cyanide (CN<sup>-</sup>) ions can strongly coordinate with iron and hence poison the Fe-containing sites. Thus, if Fe-based species are the actual active sites for ORR, the activity will diminish markedly after

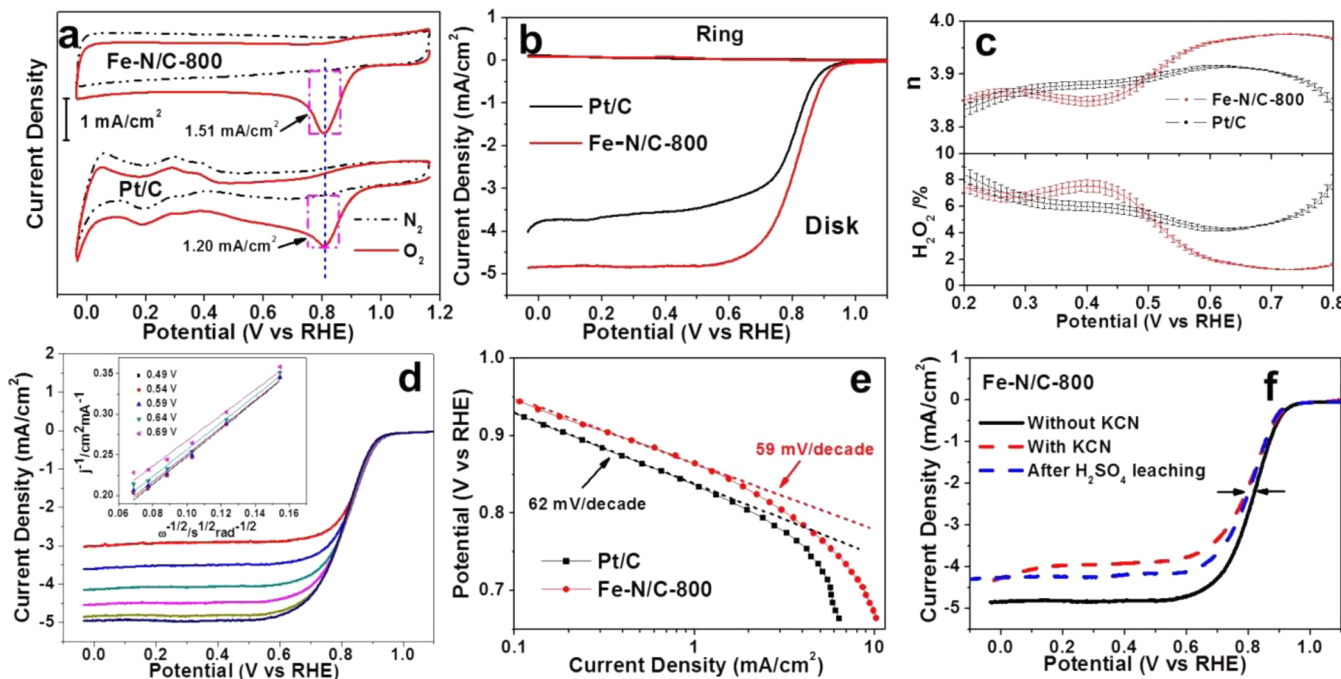


**Figure 4.** (a) Cyclic and (b) RRDE voltammograms, (c) plots of  $\text{H}_2\text{O}_2$  yield and number of electron transfer of a GCE modified with Fe-N/C-800 and Pt/C catalysts at the rotation speed of 1600 rpm. Statistic results were based on data of three independent measurements. (d) LSV curves for Fe-N/C-800 at the rotation rates of 400 to 2025 rpm; inset is the corresponding K-L plots at different potentials. (e) Corresponding Tafel plots of Fe-N/C-800 and Pt/C catalysts. (f) LSV curves of Fe-N/C-800 before (black) and after (blue)  $\text{H}_2\text{SO}_4$  leaching treatments, and in 0.1 M KOH aqueous solution with 10 mM KCN (red). All measurements were conducted at a catalyst loading of  $79.6 \mu\text{g}/\text{cm}^2$  in an  $\text{O}_2$ -saturated 0.1 M KOH aqueous solution at a sweep rate of 10 mV/s.

cyanide treatment.<sup>48</sup> Experimentally, electrochemical tests (Figure 4f) were carried out with an Fe-N/C-800 modified GCE in an oxygen-saturated 0.1 M KOH aqueous solution in the absence (black curve) and presence (red curve) of 10 mM KCN. The RDE voltammograms exhibited a 24 mV negative shift of the half-wave potential when KCN was added to the electrolyte solution, along with about 20% diminishment of the diffusion-limited currents. In another experiment, the Fe-N/C-800 catalysts were first leached in hot 0.5 M  $\text{H}_2\text{SO}_4$  ( $80^\circ\text{C}$ ) to remove metal (oxide) species before being loaded on the GCE for ORR testing. The corresponding RDE voltammogram (blue curve) exhibited a negative shift of the half-wave potential by 18 mV, and a decrease of the diffusion-limited currents by about 15%, as compared to those observed with the as-prepared Fe-N/C-800 (black curve). These results suggest that whereas Fe-containing species were likely involved in ORR, as proposed in various recent studies in the literature where the active sites in Fe-N/C were ascribed to Fe-N<sub>x</sub> moieties,<sup>44,49</sup> the contributions were small. It should be noted that the actual Fe-species in the present Fe-N/C catalysts remained unknown due to their low concentrations, yet both stable Fe-N<sub>x</sub> and chemically labile forms such as  $\text{Fe}_3\text{C}$  and  $\text{Fe}_3\text{O}_4$  were the possible products, as suggested by XPS measurements in Figure 2.<sup>50,51</sup> Furthermore, the fact that substantial ORR currents remained despite these harsh treatments (cyanide poisoning and hot  $\text{H}_2\text{SO}_4$  leaching) suggests that ORR was primarily due to iron-free active sites that arose most likely from nitrogen doping. In fact it has been reported that with graphitic-N dopants, because of the stronger electronegativity of N than that of C, the electron density of adjacent carbon nuclei will be reduced, leading to electron transfer from adjacent C to N dopants, and in return N back-donates electrons to the adjacent C p<sub>z</sub> orbitals by n-π

conjugation.<sup>52,53</sup> The donation and back-donation processes not only help form a strong chemical bond between O and C for  $\text{O}_2$  adsorption<sup>52</sup> but also facilitate  $\text{O}_2$  dissociation on the adjacent C atoms. That is, graphitic-N has been proposed to promote ORR. The formation of a mesoporous structure (Figure 1) also facilitated the transport of reaction intermediates and products, leading to enhanced ORR activity.

The durability of the Fe-N/C-800 and commercial Pt-C catalysts for ORR was then assessed and compared by chronoamperometric measurements at +0.70 V in an  $\text{O}_2$ -saturated 0.1 M KOH solution. As shown in Figure 5a, after 10,000 s of continuous operation, the commercial Pt/C electrode exhibited a rapid decrease of the voltammetric current by about 50% as compared to the initial value, indicating poor stability of the Pt/C electrode; in sharp contrast, the Fe-N/C-800 catalyst retained up to 93.3% of its original current under the same experimental conditions, which clearly demonstrated much enhanced stability of the Fe-N/C-800 catalyst for ORR. The resistance of the catalysts to methanol crossover is also of particular importance in practical applications. As shown in the inset to Figure 5a, upon the injection of 1 M methanol into the electrolyte solution, the commercial Pt/C electrode (red curve) even showed a change of sign of the voltammetric current due to oxidation of methanol on the electrode surface, and the current was gradually recovered to the negative side (ORR) but only to about 50% of that prior to methanol injection. In contrast, no noticeable change was observed of the ORR current at the Fe-N/C-800 electrode (black curve), suggesting strong tolerance to methanol crossover.

The Fe-N/C-800 catalyst also exhibited remarkable long-term stability. For instance, RDE measurements showed almost

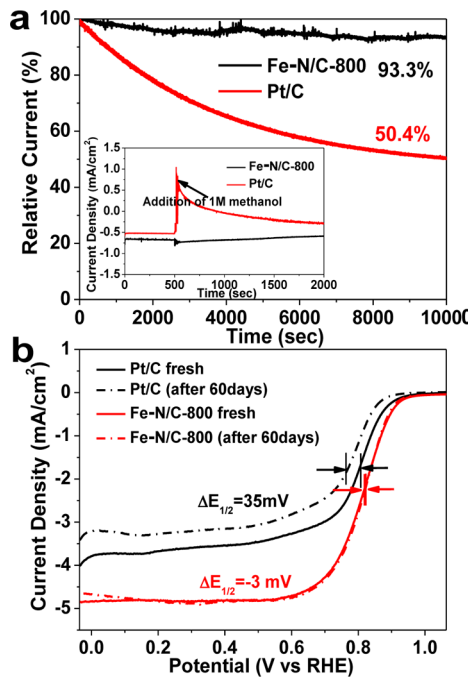


**Figure 5.** (a) Chronoamperometric curves of a GCE modified with Fe-N/C-800 and Pt/C at +0.70 V vs RHE in an O<sub>2</sub>-saturated 0.1 M KOH solution. The rotation speed was 900 rpm. Inset shows the chronoamperometric curves at +0.70 V in an O<sub>2</sub>-saturated aqueous solution of 0.1 M KOH + 1 M methanol. The rotation speed was also 900 rpm. (b) LSV curves before and after the electrode was stored in the electrolyte solution for 60 d.

no change of the ORR voltammetric currents even after the catalyst-modified electrode was immersed in the electrolyte solution for 60 d. In fact, from Figure 5b, one can see that the half-wave potential and the diffusion-limited current remained virtually unchanged (red curves). In contrast, the commercial Pt/C electrode (black curves) showed a negative shift of the half-wave potential by 35 mV and a diminishment of the limiting current by about 10%. The much enhanced durability of Fe-N/C-800 may be ascribed to the unique structure of the porous carbons: (i) the irregular sheet-like morphology not only helped prevent aggregation of the catalysts but also maintained continuous electron-transport pathways for ORR; (ii) the unique mesoporous structure of the relatively rigid carbon matrix facilitated the transport of electrolyte ions, reaction intermediates, and products;<sup>54–56</sup> and (iii) the mesoporous structure might also minimize the dissolution/agglomeration of active sites in the carbon matrix.<sup>57</sup>

It is worthy to note that the Fe-N/C-800 catalyst also exhibited apparent ORR activity in acidic media. As shown in Figure S9a, although the onset potential for Fe-N/C-800 (+0.77 V) in O<sub>2</sub> saturated 0.1 M HClO<sub>4</sub> was about 60 mV negative to that of Pt/C (+0.83 V), the limiting current of Fe-N/C-800 (4.88 mA/cm<sup>2</sup> at +0.20 V) was much higher than that of Pt/C (3.78 mA/cm<sup>2</sup>). Additionally, the average number of electron transfer for Fe-N/C-800 was determined to be 3.95, which is slightly higher than that of Pt/C (3.93) (Figure S9b). These results demonstrate that the Fe-N/C-800 catalyst shows high selectivity to the 4e<sup>−</sup> ORR in both alkaline and acidic media. Furthermore, in comparison with Fe-N/C-800 prepared at other FeCl<sub>3</sub>:2FANI feed ratios, the samples presented above at a 2:1 molar ratio were found to display the best catalytic activity for ORR (Figure S10), within the context of onset

potential, diffusion-limited current density and number of electron transfer. This might be accounted for by an optimal balance of specific surface area, active site density, and electron conductivity.

Additional control experiments were carried out with aniline instead of F2ANI. Yet the mixing of FeCl<sub>3</sub> with aniline quickly led to the formation of a cloudy suspension rather than a stable solution, and a markedly lower ORR activity was observed with the resulting porous carbons prepared in a same fashion (Figures S11–S13). Thus, aniline was not used in the present study.

## CONCLUSION

In summary, mesoporous carbons with a remarkably high specific surface area were readily prepared by controlled pyrolysis of a nanocomposite based on poly(2-fluoroaniline) within which FeO(OH) nanorods were embedded rather homogeneously in a one-pot hydrothermal synthesis. During the carbonization process the FeO(OH) nanocrystals not only acted as rigid templates to minimize collapse of the polymer matrix but also formed a large number of mesopores in the resulting carbon skeletons due to thermal decomposition and evaporation of the nanorods. XPS measurements confirmed that resulting porous carbons were codoped with both Fe and N; and electrochemical measurements showed apparent activity for ORR in alkaline media, and the samples prepared by pyrolysis at 800 °C (Fe-N/C-800) were identified as the best ORR catalysts among the series. The ORR activity was primarily ascribed to N doping with a small contribution from the trace Fe species remaining in the samples. Within the context of onset potential, number of electron transfer, specific activity, durability, and tolerance against methanol crossover, the Fe-N/C-800 sample actually exhibited much enhanced ORR activity even compared to commercial Pt/C catalysts. These results highlight the unique potential of using thermally sacrificial templates for the synthesis of highly porous carbons and the applications for ORR electrocatalysis.

## ASSOCIATED CONTENT

### S Supporting Information

Additional experimental data and discussion. This material is available free of charge via the Internet at <http://pubs.acs.org>.

## AUTHOR INFORMATION

### Corresponding Authors

\*esguili@scut.edu.cn

\*shaowei@ucsc.edu

### Notes

The authors declare no competing financial interest.

## ACKNOWLEDGMENTS

This work was supported by the National Recruitment Program of Global Experts. L.G.L. acknowledges the financial support from the Fundamental Research Funds for the Central Universities (SCUT grant no. 2013ZM0019). S.W.C. thanks the National Science Foundation for partial support of the work (CHE-1265635 and DMR-1409396).

## REFERENCES

- (1) Kang, Y. J.; Ye, X. C.; Chen, J.; Cai, Y.; Diaz, R. E.; Adzic, R. R.; Stach, E. A.; Murray, C. B. *J. Am. Chem. Soc.* 2013, 135, 42.

- (2) Proch, S.; Wirth, M.; White, H. S.; Anderson, S. L. *J. Am. Chem. Soc.* **2013**, *135*, 3073.
- (3) Zhang, C. L.; Hwang, S. Y.; Trout, A.; Peng, Z. M. *J. Am. Chem. Soc.* **2014**, *136*, 7805.
- (4) Lee, K. S.; Cho, Y. H.; Jeon, T. Y.; Yoo, S. J.; Park, H. Y.; Jang, J. H.; Sung, Y. E. *ACS Catal.* **2012**, *2*, 739.
- (5) Bing, Y. H.; Liu, H. S.; Zhang, L.; Ghosh, D.; Zhang, J. *J. Chem. Soc. Rev.* **2010**, *39*, 2184.
- (6) Tan, Y. M.; Xu, C. F.; Chen, G. X.; Fang, X. L.; Zheng, N. F.; Xie, Q. *J. Adv. Funct. Mater.* **2012**, *22*, 4584.
- (7) Ma, X. M.; Meng, H.; Cai, M.; Shen, P. K. *J. Am. Chem. Soc.* **2012**, *134*, 1954.
- (8) Chen, Z. W.; Higgins, D.; Yu, A. P.; Zhang, L.; Zhang, J. *J. Energy Environ. Sci.* **2011**, *4*, 3167.
- (9) Jaouen, F.; Proietti, E.; Lefevre, M.; Chenitz, R.; Dodelet, J. P.; Wu, G.; Chung, H. T.; Johnston, C. M.; Zelenay, P. *Energy Environ. Sci.* **2011**, *4*, 114.
- (10) Bashyam, R.; Zelenay, P. *Nature* **2006**, *443*, 63.
- (11) Liu, R. L.; von Malotki, C.; Arnold, L.; Koshino, N.; Higashimura, H.; Baumgarten, M.; Mullen, K. *J. Am. Chem. Soc.* **2011**, *133*, 10372.
- (12) Wu, Z. S.; Yang, S. B.; Sun, Y.; Parvez, K.; Feng, X. L.; Mullen, K. *J. Am. Chem. Soc.* **2012**, *134*, 9082.
- (13) Liang, H. W.; Wei, W.; Wu, Z. S.; Feng, X. L.; Mullen, K. *J. Am. Chem. Soc.* **2013**, *135*, 16002.
- (14) Lin, L.; Zhu, Q.; Xu, A. W. *J. Am. Chem. Soc.* **2014**, *136*, 11027.
- (15) Yin, H.; Zhang, C. Z.; Liu, F.; Hou, Y. L. *Adv. Funct. Mater.* **2014**, *24*, 2930.
- (16) Chung, H. T.; Won, J. H.; Zelenay, P. *Nat. Commun.* **2013**, *4*, 1922.
- (17) Serov, A.; Artyushkova, K.; Atanassov, P. *Adv. Energy Mater.* **2014**, *4*, 1301735.
- (18) Liang, Y. Y.; Wang, H. L.; Zhou, J. G.; Li, Y. G.; Wang, J.; Regier, T.; Dai, H. J. *J. Am. Chem. Soc.* **2012**, *134*, 3517.
- (19) Liang, Y. Y.; Wang, H. L.; Diao, P.; Chang, W.; Hong, G. S.; Li, Y. G.; Gong, M.; Xie, L. M.; Zhou, J. G.; Wang, J.; Regier, T. Z.; Wei, F.; Dai, H. J. *J. Am. Chem. Soc.* **2012**, *134*, 15849.
- (20) Wu, Z. X.; Lv, Y. Y.; Xia, Y. Y.; Webley, P. A.; Zhao, D. Y. *J. Am. Chem. Soc.* **2012**, *134*, 2236.
- (21) Silva, R.; Voiry, D.; Chhowalla, M.; Asefa, T. *J. Am. Chem. Soc.* **2013**, *135*, 7823.
- (22) Zhou, K.; Zhou, W. J.; Liu, X. J.; Wang, Y.; Wan, J. Q.; Chen, S. W. *ACS Appl. Mater. Interfaces* **2014**, *6*, 14911.
- (23) Zhang, P.; Sun, F.; Xiang, Z. H.; Shen, Z. G.; Yun, J.; Cao, D. P. *Energy Environ. Sci.* **2014**, *7*, 442.
- (24) Zhou, M.; Yang, C. Z.; Chan, K. Y. *Adv. Energy Mater.* **2014**, *4*, 1400840.
- (25) Liu, X. J.; Li, L. G.; Zhou, W. J.; Zhou, Y. C.; Niu, W. H.; Chen, S. W. *ChemElectroChem* **2015**, DOI: 10.1002/celc.201500002.
- (26) Jahan, M.; Bao, Q. L.; Loh, K. P. *J. Am. Chem. Soc.* **2012**, *134*, 6707.
- (27) Zhong, H. X.; Wang, J.; Zhang, Y. W.; Xu, W. L.; Xing, W.; Xu, D.; Zhang, Y. F.; Zhang, X. B. *Angew. Chem., Int. Ed.* **2014**, *53*, 14235.
- (28) Liang, C. D.; Li, Z. J.; Dai, S. *Angew. Chem., Int. Ed.* **2008**, *47*, 3696.
- (29) Wang, X.; Chen, X. Y.; Gao, L. S.; Zheng, H. G.; Ji, M. R.; Tang, C. M.; Shen, T.; Zhang, Z. D. *J. Mater. Chem.* **2004**, *14*, 905.
- (30) Tang, B.; Wang, G. L.; Zhuo, L. H.; Ge, J. C.; Cui, L. J. *Inorg. Chem.* **2006**, *45*, 5196.
- (31) Song, H. J.; Liu, L.; Jia, X. H.; Min, C. Y. *J. Nanopart. Res.* **2012**, *14*.
- (32) Liu, W. J.; Tian, K.; He, Y. R.; Jiang, H.; Yu, H. Q. *Environ. Sci. Technol.* **2014**, *48*, 13951.
- (33) Gok, A.; Sari, B.; Talu, M. *J. Polym. Sci., Polym. Phys.* **2004**, *42*, 3359.
- (34) Sharma, A. L.; Saxena, V.; Annapoorni, S.; Malhotra, B. D. *J. Appl. Polym. Sci.* **2001**, *81*, 1460.
- (35) Huang, K. Y.; Shiu, C. L.; Su, Y. A.; Yang, C. C.; Yeh, J. M.; Wei, Y.; Lee, K. R. *J. Membr. Sci.* **2009**, *339*, 171.
- (36) Geng, D. S.; Chen, Y.; Chen, Y. G.; Li, Y. L.; Li, R. Y.; Sun, X. L.; Ye, S. Y.; Knights, S. *Energy Environ. Sci.* **2011**, *4*, 760.
- (37) Qu, L. T.; Liu, Y.; Baek, J. B.; Dai, L. M. *ACS Nano* **2010**, *4*, 1321.
- (38) Maldonado-Hodar, F. J.; Moreno-Castilla, C.; Rivera-Utrilla, J.; Hanzawa, Y.; Yamada, Y. *Langmuir* **2000**, *16*, 4367.
- (39) Mao, Y.; Duan, H.; Xu, B.; Zhang, L.; Hu, Y. S.; Zhao, C. C.; Wang, Z. X.; Chen, L. Q.; Yang, Y. S. *Energy Environ. Sci.* **2012**, *5*, 7950.
- (40) Li, Q. Q.; Zhang, S.; Dai, L. M.; Li, L. S. *J. Am. Chem. Soc.* **2012**, *134*, 18932.
- (41) Chen, P.; Wang, L. K.; Wang, G.; Gao, M. R.; Ge, J.; Yuan, W. J.; Shen, Y. H.; Xie, A. J.; Yu, S. H. *Energy Environ. Sci.* **2014**, *7*, 4095.
- (42) Liu, R. L.; Wu, D. Q.; Feng, X. L.; Mullen, K. *Angew. Chem., Int. Ed.* **2010**, *49*, 2565.
- (43) Lai, L. F.; Potts, J. R.; Zhan, D.; Wang, L.; Poh, C. K.; Tang, C. H.; Gong, H.; Shen, Z. X.; Jianyi, L. Y.; Ruoff, R. S. *Energy Environ. Sci.* **2012**, *5*, 7936.
- (44) Liu, J.; Sun, X. J.; Song, P.; Zhang, Y. W.; Xing, W.; Xu, W. L. *Adv. Mater.* **2013**, *25*, 6879.
- (45) Ramaswamy, A.; Froeyen, M.; Herdewijn, P.; Ceulemans, A. J. *Am. Chem. Soc.* **2010**, *132*, 587.
- (46) Lefevre, M.; Dodelet, J. P.; Bertrand, P. *J. Phys. Chem. B* **2002**, *106*, 8705.
- (47) Nabae, Y.; Moriya, S.; Matsubayashi, K.; Lyth, S. M.; Malon, M.; Wu, L. B.; Islam, N. M.; Koshigoe, Y.; Kuroki, S.; Kakimoto, M. A.; Miyata, S.; Ozaki, J. *Carbon* **2010**, *48*, 2613.
- (48) Wang, Q.; Zhou, Z. Y.; Lai, Y. J.; You, Y.; Liu, J. G.; Wu, X. L.; Terefe, E.; Chen, C.; Song, L.; Rauf, M.; Tian, N.; Sun, S. G. *J. Am. Chem. Soc.* **2014**, *136*, 10882.
- (49) Wang, M. Q.; Yang, W. H.; Wang, H. H.; Chen, C.; Zhou, Z. Y.; Sun, S. G. *ACS Catal.* **2014**, *4*, 3928.
- (50) Schulenburg, H.; Stankov, S.; Schunemann, V.; Radnik, J.; Dorbandt, I.; Fiechter, S.; Bogdanoff, P.; Tributsch, H. *J. Phys. Chem. B* **2003**, *107*, 9034.
- (51) Wu, G.; More, K. L.; Johnston, C. M.; Zelenay, P. *Science* **2011**, *332*, 443.
- (52) Deng, D. H.; Pan, X. L.; Yu, L. A.; Cui, Y.; Jiang, Y. P.; Qi, J.; Li, W. X.; Fu, Q. A.; Ma, X. C.; Xue, Q. K.; Sun, G. Q.; Bao, X. H. *Chem. Mater.* **2011**, *23*, 1188.
- (53) Kim, H.; Lee, K.; Woo, S. I.; Jung, Y. *Phys. Chem. Chem. Phys.* **2011**, *13*, 17505.
- (54) Yang, S. B.; Feng, X. L.; Ivanovici, S.; Mullen, K. *Angew. Chem., Int. Ed.* **2010**, *49*, 8408.
- (55) Chen, D. Y.; Ji, G.; Ma, Y.; Lee, J. Y.; Lu, J. M. *ACS Appl. Mater. Interfaces* **2011**, *3*, 3078.
- (56) Liu, J.; Sun, X.; Song, P.; Zhang, Y.; Xing, W.; Xu, W. *Adv. Mater.* **2013**, *25*, 6879.
- (57) Ikeda, S.; Ishino, S.; Harada, T.; Okamoto, N.; Sakata, T.; Mori, H.; Kuwabata, S.; Torimoto, T.; Matsumura, M. *Angew. Chem., Int. Ed.* **2006**, *45*, 7063.